Neutron imaging: a new possibility for laboratory observation of hydraulic fractures in shale?

S. Roshankhah, Jason Marshall, Alessandro Tengattini, Edward Ando, V. Rubino, A. Rosakis, G. Viggiani, Jose E. Andrade

Géotechnique Letters **00**, 1–10, http://dx.doi.org/10.1680/geolett.XX.XXXXX

Neutron Imaging: A New Possibility for Laboratory Observation of Hydraulic Fracture in Shale?

SHAHRZAD ROSHANKHAH*, JASON MARSHALL*, ALESSANDRO TENGATTINI†, EDWARD ANDO‡, VITO RUBINO§, ARES J. ROSAKIS§, GIOACCHINO VIGGIANI‡ and JOSE E. ANDRADE*

Hydraulic fracture, the creation of fractures by high pressure fluid injection into a solid medium, is of interest to enhance the permeability of rocks. This complex 3D hydro-mechanical process, however, has only been studied in the lab by boundary measurements or acoustic techniques with low spatio-temporal resolutions until now. In this paper, we present direct, full-field, high spatial resolution, and near real-time visualization results of hydraulic fracture generation and propagation in prismatic specimens of Marcellus shale rock under *in-situ* conditions (3 km depth, plane strain). We test PMMA (Poly-Methyl Methacrylate) specimens as well under the same conditions to highlight the importance of internal structure on the response of the tested rock. The results reveal a complex interaction between the injected fluid, the pre-existing natural fractures in shale's structure, and the hydraulically-induced fracture highlighting the governing role of rock fabric even under high stresses. These measurements are possible due to the unique sensitivity of neutrons to water. Besides the intrinsic interest of the results presented, this exploratory investigation highlights the potential of neutron imaging in elucidating the evolution of fluid flow and fluid-driven fractures, as x-rays have done for the evolution of solid structure only. Further, understanding of the mechanics of fracking will lead to development of more accurate hydro-mechanical constitutive models thus enabling the design of field operations with higher efficiencies.

KEYWORDS: Hydraulic fracturing, Heterogeneous media, High resolution imaging, neutron radiography, Natural fractures, Shale rock

INTRODUCTION

The Concept of hydraulic fracturing has been around for several decades, and it is encountered in many important geo-energy and geo-environmental applications, from stimulation of deep unconventional oil and gas (Economides & Nolte (2000)), geothermal energy (Legarth *et al.* (2005)), and heavy oil (Davletbaev *et al.* (2014)) reservoirs, to geological energy storage (Bauer *et al.* (2013)), waste disposal (Tsang *et al.* (2015)), and CO_2 sequestration (Verdon *et al.* (2010)). However, there is still a lack of understanding of the underlying physics. As a result, it is reported that field operations underutilize about 30% of the targeted subsurface resources (Lecampion & Desroches (2015)). This is mostly due to the complexity of the process, where there is a multi-phase fluid interaction with heterogeneous, anisotropic, inelastic, low-permeability rocks, whose rheology is highly non-linear. Models that we currently use to predict the response of subsurface geomaterials to hydraulic stimulation have been actually developed for materials with simple properties (e.g., homogeneous, isotropic, linear, and elastic), thus they result in large errors. Clearly, there is an urgent need to realistically quantify this complex phenomenon. Direct and through-depth visualization of these multi-physics phenomena in real rocks, under realistic boundary conditions, and with high spatio-temporal resolution can transform our scientific understanding of hydraulic fracture phenomena and provide us with necessary tools for direct modeling.

Experimentally, progress has been made in the past on visualization of hydraulic fracture propagation in model materials that are transparent to visible light (i.e., PMMA); yet, these materials are homogeneous and impervious, and

Manuscript received. . .
Published online at www.geotechniqueletters.com
*Department of Mechanical and Civil Engineering, Division of Engineering and Applied Science, California Institution of Technology, 1200 E. California Blvd., MC 104-44, Pasadena, 91125, CA, USA. Tel.: 6263954394, Email: shroshan@caltech.edu, Email: jmarshal@caltech.edu, Email: jandrade@caltech.edu
†Institute Laue-Langevin, 71 avenue des Martyrs - CS 20156, 38042 Cedex 9, Grenoble, France, Email: alessandro.tengattini@3sr-grenoble.fr
‡Institute of Engineering, Univ. Grenoble Alpes, Laboratoire 3SR, Domaine Universitaire, BP53, 38041 Grenoble Cedex 9, Grenoble, France, Email: edward.ando@3sr-grenoble.fr, Email: cino.viggiani@3sr-grenoble.fr
§Aerospace Laboratories, California Institute of Technology, 1200 E. California Blvd., MC 105-50, Pasadena, CA, USA, Email: vito.rubino@caltech.edu, Email: arosakis@caltech.edu

their behavior can be reasonably approximated by linear elastic fracture mechanics (LEFM) coupled with lubrication theory (e.g., Bunger & Detournay (2008) Lecampion *et al.* (2017) Bunger *et al.* (2013)). Natural rocks do not fit in these assumptions. Indirect methods such as acoustic emissions have been used to infer the width and length of hydraulic fractures in rocks (e.g., Groenenboom & Fokkema (1998)), but they do not provide information about interactions between the generated hydraulic fracture with the complex network of anisotropies. Moreover, the spatial resolution of these methods are low compared to characteristic length of the fracture phenomenon, e.g., wavelength is at least two orders of magnitude larger than the width of detected fractures. There are numerous studies showing that both boundary conditions and pattern of pre-existing natural fractures (flaws) influence the involved physical processes upon hydraulic fracturing and subsequently the geometry and extent of resulted fractures in natural rocks (e.g., Warpinski & Teufel (1987) da Silva & Einstein (2018)).

At the field scale, geophysical methods have been developed to investigate characteristics of hydraulic fractures by visualizing the structure of subsurface rock masses before and after hydraulic treatment. For example, microseismic techniques (Juhlin (1995)Williams-Stroud *et al.* (2010)), radar (Day-Lewis *et al.* (2002)Olsson *et al.* (1992)), tracer tests (Maloszewski *et al.* (1999)), and active and passive acoustic emissions (Meng & De Pater (2011)Williams & Johnson (2004)) have been prominently used. The highest spatial resolution of these methods, however, is in the order of a meter and cannot capture the fine fabric of the rock mass that governs its global hydro-mechanical behavior. As an indirect *in situ* method, the frequency and aperture of main joints have been inferred from fluid flow and pressure data (Dershowitz *et al.* (1998)Nolte (1991)). The accuracy of these estimations is very low such that they can justify neither the stimulated reservoir volume nor the production rate (Maxwell *et al.* (2011)).

In this work, we present results of visualizing the process of hydraulic fracture in extremely low permeability rocks (Marcellus shale) using a high-power flux neutron source (NeXT instrument, Grenoble, France). These results provide a proof of concept, reminiscent of the initial results obtained in granular soils or dry fractures in rocks with x-ray computed tomography (X-ray CT) (Viggiani *et al.* (2004)Jia *et al.* (2014)). X-ray CT has provided access to the mechanical properties of geomaterials by quantifying the pore scale phenomena (e.g., Kawamoto *et al.* (2018) Sun *et al.* (2011)). Those observations enabled a new generation of predictive computational models. We claim that neutron imaging has a similar potential by providing access to the evolution of the fluid front in near real-time, something that X-ray CT struggles to do because of its insensitivity to hydrogen atoms (Frash *et al.* (2016)). This method lends itself as a potential high-impact tool to provide quantitative access to important parameters of hydraulic fracture including the propagation path and speed in heterogeneous media in the near future.

EXPERIMENTAL SETUP

For laboratory physical models of hydraulic fracture to be dimensionally consistent with the field condition, we must use specimens with low fracture toughness and low permeability or inject a liquid with a high viscosity and with a lower rate than that in field treatments (De Pater *et al.* (1994)). Because of the distinct hydro-mechanical behavior of natural rocks (e.g., De Pater & Beugelsdijk (2005) Potluri *et al.* (2005) Gale *et al.* (2007) Dahi-Taleghani & Olson (2011) among many others) from isotropic and homogenous artificial porous samples (plaster or cement paste samples previously used in experimental studies, e.g., Van Dam *et al.* (2000)), we directly test Marcellus shale samples. The results presented in this study are obtained by injecting regular water (η_w=0.001 Pa.s) into shale specimens as a proof-of-principle. We are planning to inject a high viscosity liquid with no suspended solid particles in our future experiments.

Testing Materials and Specimen Preparation

In this work, Marcellus shale and PMMA specimens of size $100 \times 100 \times 25\ mm$ are prepared (see Figure 1a). While our main interest is to investigate the fracture behavior in heterogeneous materials, especially, natural rocks such as shale, we also tested PMMA. This helps to understand the degree of dominance of natural fractures in shale structure when we compare its response to homogeneous and isotropic PMMA. Shale's mechanical properties, including fracture toughness (average values), are similar to those of PMMA (Sone & Zoback (2013)Christman (1972)), but the latter is more ductile. Another advantage of PMMA as a model material is its optical transparency, which allows visual assessment of damage associated with the hydraulic crack propagation through the bulk without the use of more sophisticated techniques.

Marcellus shale is a brittle, highly anisotropic material. Anisotropy is present both in mechanical and poro-mechanical properties due to the presence of three sets of mutually perpendicular fractures with different geometric characteristics in its internal structure. One set is usually the horizontal or sub-horizontal bedding planes, which occur due to the sedimentation process creating layers of couple millimeters thick. The other two sets are tensile fractures orthogonal to bedding planes as a result of applied vertical maximum principal stress in the earth's crust. Large faces of the shale specimens prepared for this study are parallel to the bedding planes.

A hole with a diameter of 6.4 mm is drilled through the specimen thickness at the center of the large faces. A 1.6 mm-long by 0.8 mm-wide notch (blunted tip) is manually sawed along the borehole wall at the top (throughout the specimen thickness) such that its plane is perpendicular to the small top and bottom faces and parallel to the small lateral sides of the specimen (Figure 1a).

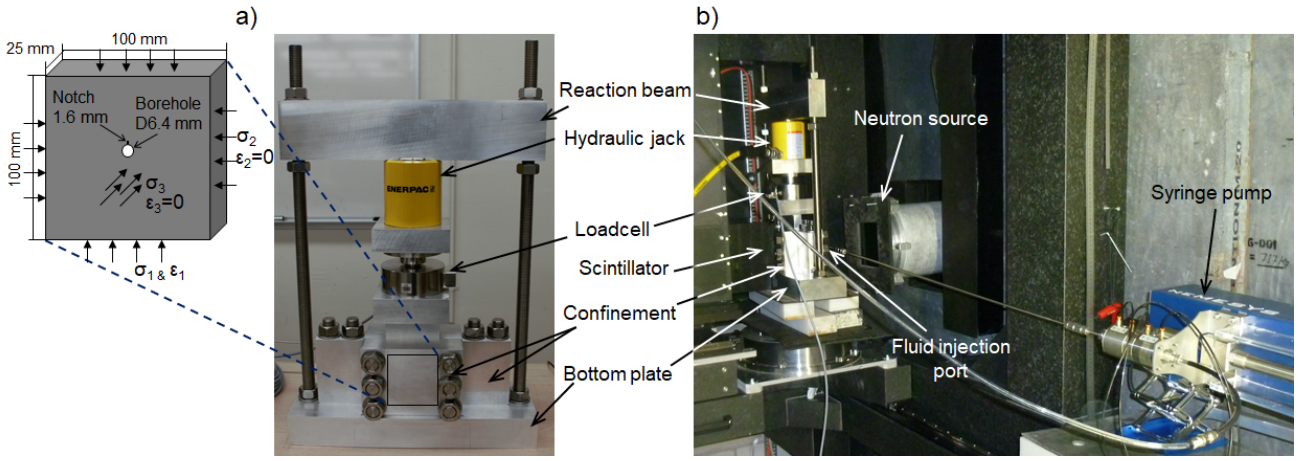

Fig. 1. a) The loading frame, confining jacket, and schematic view of a prepared specimen with imposed boundary condition (plane strain). b) Experimental device in the neutron chamber (Laue-Langevin, Grenoble, France). Axis of the neutron beam is perpendicular to large faces of the loaded specimen. Side view of the loading frame is shown, and various parts of the apparatus are marked.

Loading Frame and Instrumentation

We designed and built a frame to vertically load a prismatic rock specimen and laterally confine it in a rigid aluminum jacket providing plane strain condition (Figure 1a). The deformation of aluminum plates under induced lateral loading (per elasticity) is over an order of magnitude lower than the aperture of the hydraulic fracture (approximate values per LEFM), thus the assumption of zero lateral strain condition is valid. A force transducer is placed in series between a hydraulic cylinder and a loading plunger to record the vertical load applied on top of the specimen.

A high-pressure stainless-steel tube (6.4 mm OD, 3.2 mm ID) is inserted through the center of one of the lateral plates confining the large faces. The tube is inserted 19 mm into the specimen's wellbore. An ultra-high-pressure syringe pump injects water (could be any specified liquid) with a constant flow rate (is set via pump's software) into the specimen via the injection tube. The fluid pressure is measured by the pump's built-in pressure transducer, and it is recorded by its data acquisition system. A face-sealing circular O-ring is installed on the internal face of each lateral plate confining the large faces to seal the injecting area around the borehole with the aid of a silicon-based high vacuum grease. This configuration (face-sealing O-rings and grease on large contacting surfaces) decreases the friction on the large lateral faces of the specimen that would otherwise prevent complete transfer and uniform distribution of the vertical stress throughout the specimen's vertical profile. Additionally, all surfaces of specimens and contacting faces of confining plates are machined with a mirror finish to decrease the friction between the contacting surfaces.

High-resolution process monitoring technique: Neutron Imaging

We use neutron radiography to monitor the fluid flow in the rock specimen during high-pressure fluid injection and neutron tomography to visualize the state of the specimen after the test. Figure 1b shows the experimental device in the neutron-imaging chamber. Large faces of the specimen are placed perpendicular to the neutron source axis.

Neutron radiography follows the same principle as X-ray radiography. Both of these types of radiation travel through matter and are generally attenuated according to the well-known Beer-Lambert law. In short, the intensity of the detected "full-beam" (with no sample in place) is used to normalize the beam detected with the sample in place giving a "radiography," i.e., field of transmission of the beam through the sample in the direction of the beam. Tomography means acquiring radiographies at a number of different angles allowing the field of attenuation to be reconstructed in 3D.

The main difference between neutron and X-ray radiation is the attenuation coefficient of different materials: for X-rays, attenuation increases with density, whereas for neutrons there is no hard-and-fast rule but some light elements such as hydrogen and lithium have large attenuation coefficients, making them easy to be detected. Neutrons are very suitable, therefore, for detecting water (Perfect *et al.* (2014)), but there is a further bonus: some materials with good mechanical properties have very low attenuation coefficients, making them ideal pressure vessels. To exploit the latter fact, the lateral plates confining the specimen are made of 6061 aluminum alloy in this study.

The neutron beam has been collimated with a 15 mm pinhole and with around 10 m propagation distance as an optimal point to maximize resolution and neutron flux in the testing conditions. Downstream of the experiment, a 100-micron thick LiF scintillator converts the neutron beam into visible light, which is captured by an s-CMOS camera with 2048×2048 pixels and an exposure time of 700 ms (this imaging rate can be improved 20 times with the currently available technology to acquire an image in every 35 ms). The radiogram of the apparatus on the scintillator is $100 \times 100\ mm$ in size such that the corresponding pixel size in the acquired images is ~$50\ \mu m/px$.

EXPERIMENTAL PROCEDURE AND RESULTS

We present here the experimental procedure and results of four tests conducted on PMMA specimens and four tests on Marcellus shale specimens. The testing specimen is first placed in the loading apparatus inside the neutron-imaging chamber. The lateral confinement is set; the vertical loading equipment (pressure booster to the hydraulic cylinder) and the injection equipment (syringe pump to the injection port) are then connected. The vertical stress on the specimen is increased gradually (in approximately one minute) until it reaches 68 MPa. This stress is equivalent to the overburden stress at about 3 km depth (average depth of shale gas formations). The syringe pump is turned on few minutes after reaching the maximum stress allowing stress equilibration in the specimen.

In our experiments, the pump is set to inject regular water at a specified constant flow rate, Q=3, 6, or 12 ml.min^{-1}, into the specimen. When the pressure reaches a critical value, fracture occurs. Figure 2a shows the plane strain hydraulic fracture created in a PMMA specimen. Pressure histories of four PMMA specimens are presented in Figure 2b (two tests are conducted with Q=6 ml.min^{-1}).

The test procedure and injected water flow rates are the same for shale specimens. Figure 3a shows the pressure profiles for tests on shale. The trends are similar to a typical pressure signature observed in the field (Figure 3b). These results are interpreted in discussion section.

Figure 4 shows a neutron image of a hydraulically fractured shale specimen initiating from both top and bottom of the wellbore. A video constructed from successive neutron radiographies (Movie S2 in the Supporting Information) shows the evolution of a vertical hydraulic fracture extending from top and bottom of the borehole and then activating a natural fracture, which accumulates water, and it is seen at the top left corner of the video.

The presence of natural fractures is inferred from the radiographs, and it is better seen in 3D by neutron tomography that also shows the bedding planes parallel to large faces. A neutron image is shown in Figure 5a, and a video of the specimen tomography after the hydraulic fracture is available via Movie S3 in the Supporting Information. A weakened plane parallel to the large faces is observed around the middle of the specimen thickness after the hydraulic fracture (Figure 5b). All shale specimens are inspected after the hydraulic fracturing tests with opened bedding planes detectable with a naked eye as well as in tomographs. The dilated plane is suspected to be the same feature that accumulated water in it after hydraulic fracture occurred (captured in Movie S2 in the Supporting Information). When the specimen is squeezed across the large faces, water is forced out of the fracture plane (Figure 5c), confirming that the dilated fracture contains water. Natural fractures filled with different clay minerals can be seen also in Figure 5d, which is a cracked open specimen from a dilated bedding plane.

DISCUSSION

Results of the experimental study reported above are discussed next. Because we did not inject liquids with scaled viscosity (high), the results of these experiments are not quantitatively representative of the field condition, but they show several important characteristics about the hydro-mechanical behavior of natural rocks subject to hydraulic stimulation. The measured maximum pressures for PMMA specimens are close to the breakdown predictions derived from linear elastic fracture mechanics (LEFM) solutions (see Text S1 in the Supporting Information for detailed calculations). The range of breakdown pressure in these calculations is obtained only based on the common range of PMMA's mechanical properties because the fracture propagation regime in this impermeable material subject to low injection flow rates is toughness-dominated, and thus it is mostly independent of the flow rate (Detournay (2016)). These results show that high-pressure fluid injection in homogeneous and isotropic materials such as PMMA produce simple fracture geometries, i.e., the fracture initiates from the pre-defined notch and propagates exactly in the expected orientation (vertical) according to the imposed plane strain boundary conditions (Hubbert & Willis (1957)).

In shale specimens, however, the hydraulic fracture is initiated in both top and bottom sides of the wellbore although we created one notch only on top; its orientation is not always exactly vertical but sometimes sub-vertical; and its propagation path deviates from the initial fracture plane (as captured by neutron radiography, Figure 5b, and Movie S2 in the Supporting Information). We attribute these observations to the presence of natural fractures in the shale structure that interact with the hydraulic fracture, redistribute the stresses, interfere in the mechanism of energy dissipation, cause mixed-mode fracturing mechanism, and propagate in a tortuous path by activating natural fractures. Note that these phenomena govern the behavior even under very high stresses contrary to the common belief that behavior of natural geomaterials under high stresses can be estimated with that of simple materials.

The governing role of the heterogeneous internal structure of shale specimens is also seen in their pressure histories. Comparing pressure signatures of the two types of materials tested in this study, we observe that the two series are neither qualitatively nor quantitatively similar to each other although the average of their mechanical properties are similar. The breakdown pressure for PMMA is fairly predictable by LEFM solutions, but it is not the case for shale (Text S1 in the Supporting Information). The assumptions for these simple solutions (linear, elastic, homogeneous, and isotropic) are not

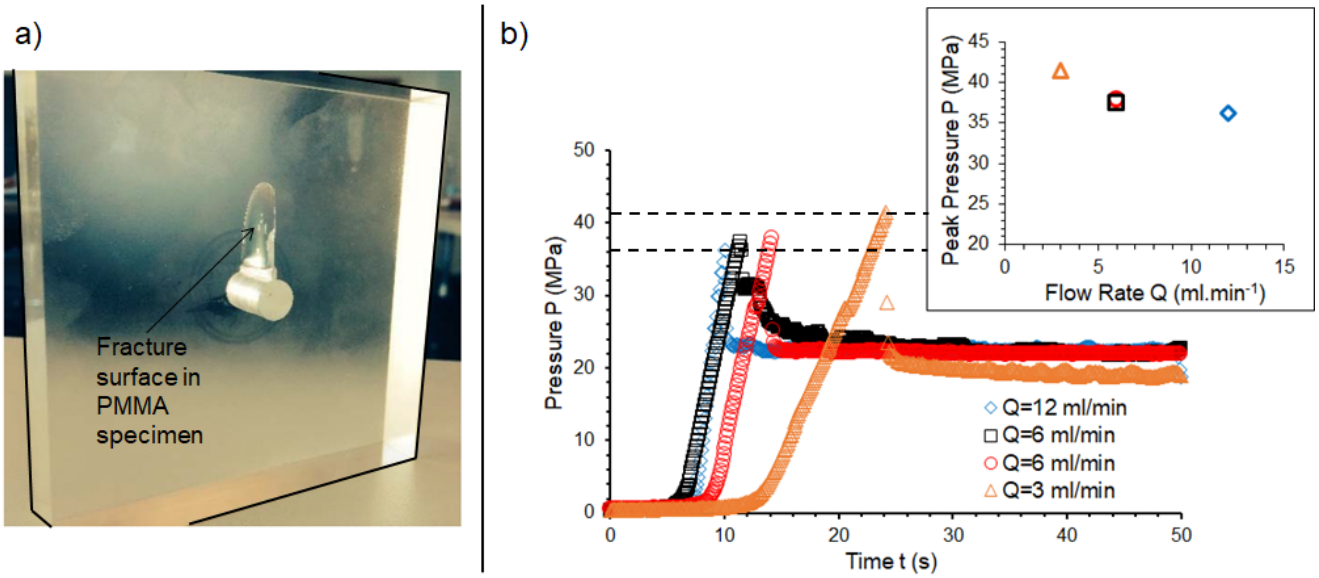

Fig. 2. Results of hydraulic fracture tests on PMMA. a) A typical fracture surface in a PMMA specimen. Only one hydraulic fracture is initiated at the tip of the predefined notch along the borehole wall, where the maximum tensile stress is concentrated according to elasticity theory, and it propagates vertically upwards in the direction of the maximum compressive stress. The shape of the generated hydraulic fracture is identical in all tests. This image corresponds to Q=6 ml.min^{-1}. b) Fluid pressure histories, where a sharp increase in pressure followed by formation of a fracture, a peak pressure near 40 MPa, and a subsequent drop in fluid pressure are recorded. Specimens are fractured hydraulically by injecting water at constant flow rates of 3, 6, and 12 ml.min^{-1}. The measured breakdown pressure (36-41 MPa) is within the predicted range provided by LEFM solutions assuming common fracture toughness and Poisson's ratio for PMMA (K_{Ic}=1.05-1.55 MPa.m$^{0.5}$ and ν=0.33); refer to Text S1 in the Supporting Information for detailed calculations and discussion section for brief interpretation of measured data. The slight variation of breakdown pressure with fluid flow rate (inset graph) must reflect the variation in properties of PMMA specimens.

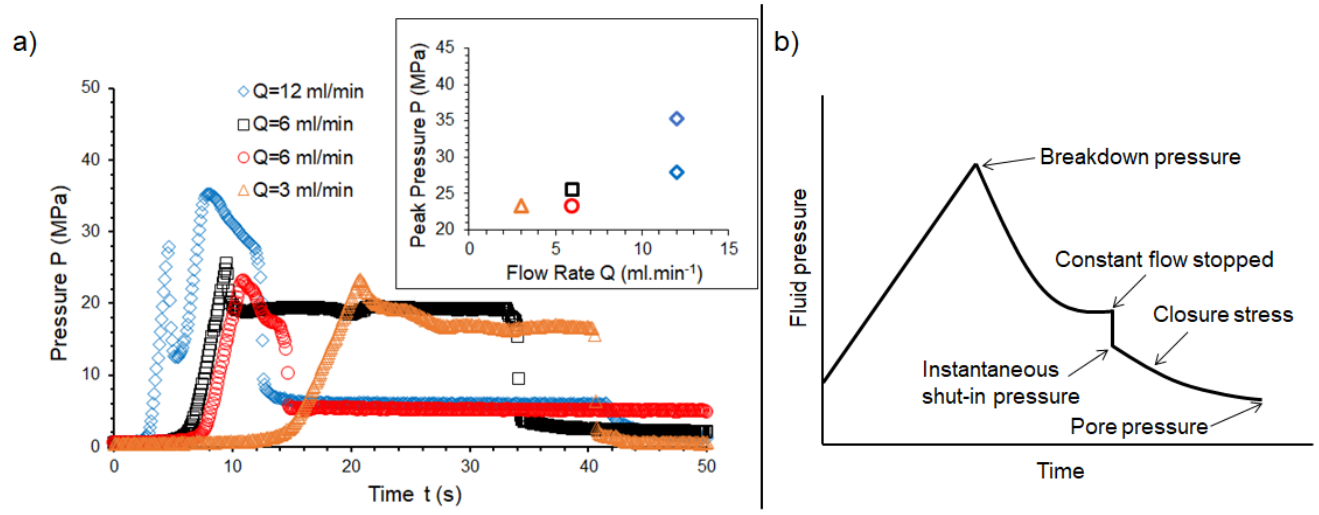

Fig. 3. Results of hydraulic fracture in shale specimens. a) Fluid pressure histories for four shale specimens hydraulically fractured by injecting water at constant flow rates of 3, 6, and 12 ml.min^{-1}. Maximum fluid pressures are measured around 23 - 35 MPa followed by a clear dropdown (reminiscent to field observations). Refer to Text S1 in the Supporting Information for predicted breakdown pressure for shale per LEFM (7-47 MPa). Given the anisotropic structure of shales, LEFM assumptions are invalid for them, which is evidenced by very different responses obtained for various specimens, even for those fractured with the same flow rates. b) Typical pressure history observed during hydraulic fracture operations in the field, with a steady pressure buildup followed by the generation of hydraulic fractures, maximum pressure (Song *et al.* (2001)), and a sharp drop in pressure and its dissipation (Economides & Nolte (2000)).

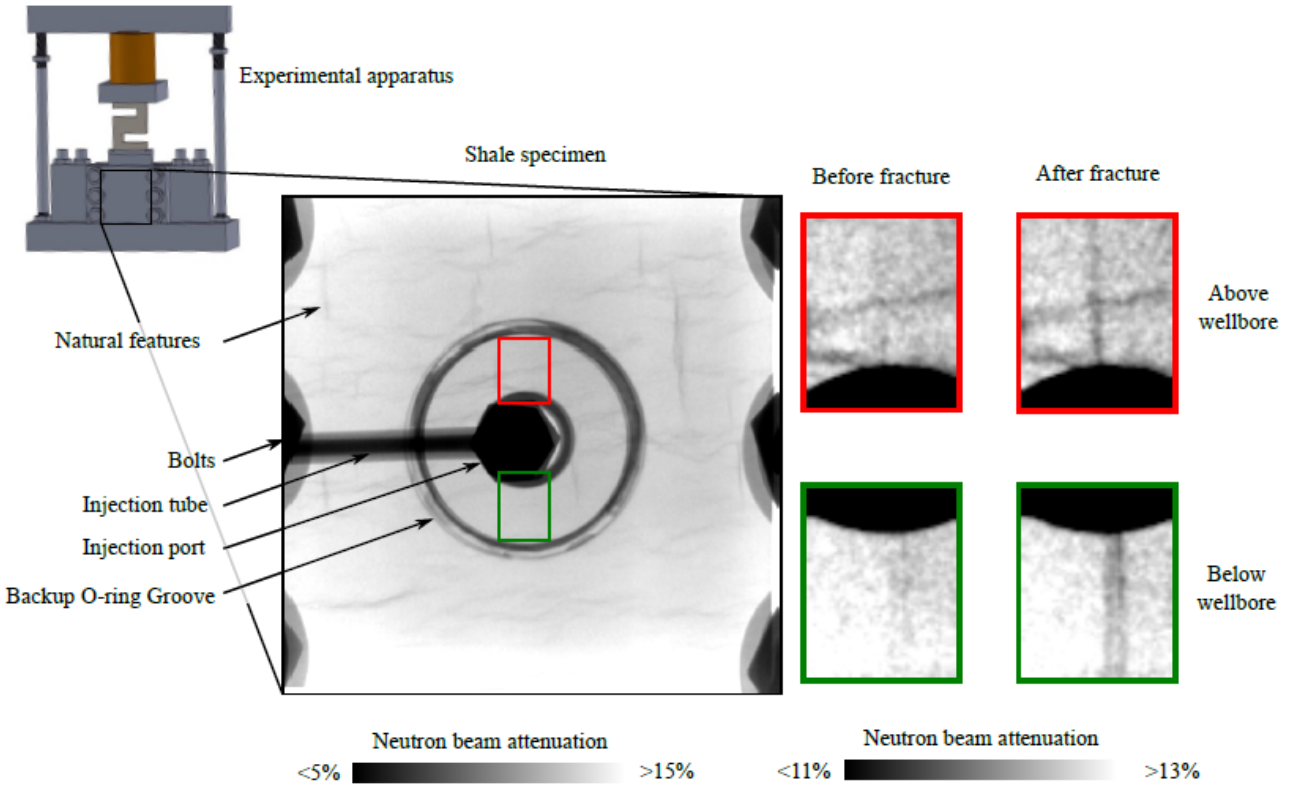

Fig. 4. Typical neutron radiography image of a shale specimen during hydraulic fracture process under *in situ* conditions. This image corresponds to the hydraulic fracture generation in shale with flow rate of Q=6 ml.min^{-1}. The un-fractured sample is captured before the peak pressure and the fractured sample is captured immediately after the peak pressure. The time history of images (see Movie˜S2 in the Supporting Information) shows the fracture process starting at the borehole with fractures initiated in the direction of the maximum compressive stress of 68 MPa, equivalent to a 3 km depth. It is interesting to note that the fracture surface bisects the natural features present above the borehole.

valid for natural heterogeneous materials because the fluid-solid interaction is more complex in porous and pre-fractured rocks.

Specifically, the peak pressure increased with flow rate for the shale samples, while it decreased with flow rate for PMMA samples. Our interpretation is that properties of the rock change with different rates upon fluid injection with different flow rates. That is, the medium around the injection borehole fails under a lower pressure when it becomes liquid-saturated, and injection with lower flow rate favors a slower pressure rise and more fluid leak-off to surrounding pores and natural features. These processes offer simple explanations for increasing breakdown pressure with increasing flow rate in shale. In an impermeable material like PMMA, the behavior is not very much flow rate-dependent. Therefore, the slight scatter in its P_b, may be attributed to the scatter in properties of this synthetic material.

Furthermore, none of the shale specimens show the same breakdown pressures, and the shape of their transient pressure dissipation responses differs for even specimens with the same injecting flow rate. This shows the great variability in geomaterials' internal fabric and again the dominance of fabric on the behavior. Even when we increased the fluid injection flow rate (Figure 3a - Q = 12 ml.min^{-1}) to suppress the influence of fluid leakage to the pores and fractures in shale so that the energy dissipation occurs mostly through the generation of new surfaces (fracture toughness) instead of viscous fluid flow, i.e., forcing shale to behave more like PMMA, the effect of internal structure of the rock still dominates the process such that two peaks are recorded in the pressure history.

A bedding plane is activated upon hydraulically fracturing the shale specimen, which provides a path for water to rapidly permeate through the specimen. Natural fractures in rocks have a rough surface (tensile genesis), but they are usually closed with matched surface asperities. The significantly increased fluid conductivity of the activated bedding plane (observed in neutron images in this study) compared to the rock mass confirms the induced opening, shear slippage, and shear-induced dilation on natural fractures because of the formation of a hydraulic fracture in their vicinity (Rutqvist & Stephansson (2003)). Any slight differential displacement (shear) imposed on walls of a natural fracture creates a mismatch between joint surface asperities and increases the fracture aperture, thus it exponentially increases its hydraulic conductivity (according to cubic law - Zimmerman & Bodvarsson (1996)). This mechanism is irreversible and generates self-propped fractures that remain productive even after pressure shut-in (e.g., Mayerhofer *et al.* (1997)).

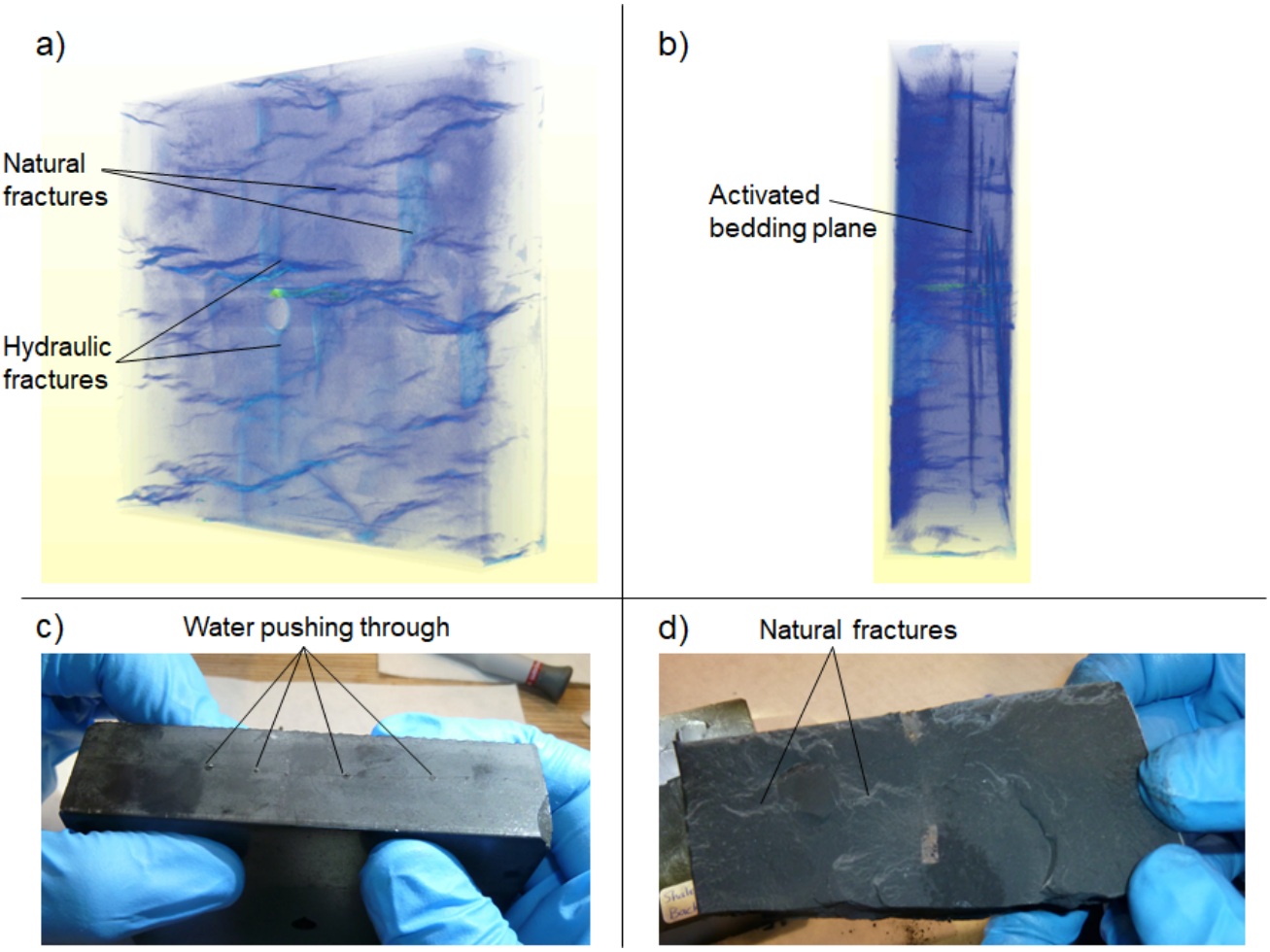

Fig. 5. a) Neutron radiography of shale specimen before hydraulic fracturing. Image shows rich heterogeneity with existing natural fractures. b) Neutron radiography of shale specimen after hydraulic fracturing. An activated natural feature (a bedding plane) following the generation of a hydraulic fracture (with planes perpendicular to one another). Also refer to videos V1 and V2 in the supporting materials for constructed neutron radiography and tomography, which show opening of the bedding plane during and after fracturing, respectively. c) Visual confirmation of a bedding plane activated due to the hydraulic fracture process. The plane has a rough surface. d) Visual confirmation that the activated natural feature serves as an outlet for water after hydraulic fracture. This feature was closed before formation of the hydraulic fracture, however, an opening, shear slippage, and shear-induced dilation are imposed on it upon generation of the hydraulic fracture that significantly increases its fluid conductivity.

In these series of experiments, we did not calculate the crack tip speed because it would be consistent with the field conditions only when we scale the injection fluid viscosity and flow rate. If we assume the fracture growth rate as small as 1 $m.s^{-1}$ (Detournay (2016)), to record the position of the crack tip at least at two points x mm apart, we would need to take images with recording rate of $1/x$ fps (frames per second). We are able to improve the current recording rate (an image per 700 ms≡1.4 fps) by 20 time with the available technology, therefore, achieving 29 fps and capturing the tip at two points 35 mm apart in the next series of our experiments.

SUMMARY AND CONCLUSIONS

Current models are unable to accurately predict the behavior of geomaterials subject to hydraulic fracturing because they have been developed with over-simplifying assumptions about material properties, to which natural rocks do not abide. It is clear that by better understanding the multi-phase and multi-scale physics of the involved phenomena, the design and implementation of hydraulic stimulation can be improved; specifically in terms of higher energy efficiency and lower environmental impact. Enabling these improvements, requires capturing the coupled hydro-mechanical processes taking place in natural rocks via scaled, highly controlled, and heavily instrumented experimental studies. In this article, we introduced an experimental setup that allows the consistent generation and stable propagation of hydraulic fractures in natural rocks under high stresses (68 MPa≡3 km deep, the average depth of shale gas reservoirs). We used water to fracture Marcellus shale and PMMA specimens. The flow rate and viscosity of the fracturing liquid are controllable so that in the future we can scale the process to field conditions by injecting more viscous liquids. In these experiments, we gather direct and high-resolution information about the hydraulic fracture process. The new neutron imaging instrument ”NeXT” in

Grenoble, France, allowed us to capture fractures before (pre-existing), during, and after the hydraulic fracture process in shale. The ability to see fluid flow within a test sample is particularly noteworthy providing us a tool to get closer to the idea of transparent earth. There are several important points to take away from these results:

- The use of neutron imaging technique allows us to capture hydro-mechanical interactions between hydraulic fractures and pre-existing natural features.
- Integrating visual observations obtained from the neutron images and data obtained from installed transducers (force, deformation, and pressure) on specimens in our loading device allows quantification of the hydraulic fracture process in natural materials under *in-situ* conditions.
- These results reveal the governing role of rocks' internal structure even under high stresses. Capturing these complex 3D fracture processes poses significant challenges for physical and numerical models to simulate.
- Some potential future investigations with the developed experimental setup include the effect of fracturing fluid viscosity and flow rate, and different mechanical boundary conditions on the path, morphology, and speed of hydraulic fracture in heterogenous media. We can also directly explore the influence of natural fractures' type and pattern in various rocks by extending this study to investigate the behavior of granitic rocks, which are found in hot dry rock formations. Little modifications will allow us to investigate the thermo-hydro-mechanical behavior of various rock masses.
- Overall, the use of neutron imaging technique appears uniquely suited to elucidate the underlying physics of hydraulic fracture with a vast range of potential applications.

SUPPORTING INFORMATION

This section contains calculations to predict breakdown pressure of PMMA and shale specimens. Additionally, captions for videos referenced in the main document are presented.

Text S1: LEFM solution for breakdown pressure

Assuming an elastic, homogeneous, isotropic, impermeable solid under a plane strain condition, we study the problem of imposed fluid pressure in a circular hole with radius R [m] featuring a vertical notch with length a [m], and we aim to determine the breakdown pressure P_b [MPa], the pressure level at which failure occurs. The geometrical and loading configuration is sketched in Figure 1a of the main article. The specimen is subjected to compressive loading σ_1 [MPa] in the vertical direction, and it is confined laterally in both of the other two orthogonal directions. The normal stresses along x_2 and x_3 directions can be expressed as $\sigma_2 = \sigma_3 = \kappa\sigma_1$, where $\kappa = \nu/(1-\nu)$, and ν is the Poisson's ratio, by assuming linear elastic constitutive laws and by imposing the boundary conditions $\varepsilon_2 = \varepsilon_3 = 0$.

The breakdown pressure is estimated via the following relationship derived from linear elastic fracture mechanics (LEFM) solutions by computing the stress intensity factor as a function of the pressure and equating it to the fracture toughness, at breakdown. The stress intensity factor K_I[MPa.m$^{0.5}$] is determined using the superposition principle and known solutions to crack problems (Tada *et al.* (2000)Gdoutos (2006)). The pressure at breakdown is the pressure level attained when the stress intensity factor reaches the fracture toughness K_{Ic} [MPa.m$^{0.5}$], and it can be expressed as:

$$P_b = \frac{K_{Ic}+\kappa\sigma_1\sqrt{\pi a}\left[\left(1-\frac{1}{\kappa}\right)F_o^\sigma(s)+\frac{1}{\kappa}F_1^\sigma(s)\right]}{\sqrt{\pi a}\left[(1-\lambda)F_o^P(s)+\lambda F_1^P(s)\right]} \quad (1)$$

where s is a geometrical parameter defined as:

$$s = \frac{a}{a+R} \quad (2)$$

F_1^σ, F_o^σ, F_1^P, and F_o^P are following functions of s:

$$F_1^\sigma(s) = 2.243 - 2.64s + 1.352s^2 - 0.248s^3 \quad (3)$$

$$F_o^\sigma(s) = \left[1 + 0.2(1-s) + 0.3(1-s)^6\right]F_1^\sigma(s) \quad (4)$$

$$F_1^P(s) = 1 + (1-s)\left[0.5 + 0.743(1-s)^2\right] \quad (5)$$

$$F_o^P(s) = \left[1 + 0.2(1-s) + 0.3(1-s)^6\right]F_1^P(s) \quad (6)$$

and λ is a factor ($0 \leq \lambda \leq 1$) showing that the fluid pressure inside the notch may be less than or equal to the fluid to the fluid pressure inside the hole. We assume $\lambda = 1$.

Geometric parameters and the vertical stress in our experiments, shown in Figure 1a: a=1.6 mm, R=3.2 mm, σ_1=68 MPa.

For PMMA: ν=0.327 (Christman (1972)) and K_{Ic} (for quasi-static crack propagation) = 1.05-1.55 MPa.m$^{0.5}$. The lower bound in the given range is the average of values measured by several methods as reported by (Choi & Salem (1993)) and the upper bound is reported by (Weerasooriya *et al.* (2006)). Also, K_{Ic}=3.27 MPa.m$^{0.5}$is reported by (Weerasooriya *et al.* (2006)) for dynamic crack propagation. Predicted breakdown pressures for PMMA given the above-mentioned values of ν and K_{Ic} are presented in Table 1.

Table 1. Fracture toughness and predicted breakdown pressure for PMMA.

K_{Ic} [MPa.m$^{0.5}$]	1.05	1.55	3.27
P_b [MPa]	36	41	56

The measured breakdown pressure for all of the tested PMMA specimens fall between the predicted pressure for quasi-static fracture propagation (36-41 MPa).

For shale:ν=0.15-0.4 (Sone & Zoback (2013)). K_{Ic}=0.47-0.72 MPa.m$^{0.5}$. The lower bound in the above range is reported for Marcellus shale by (Lee *et al.* (2015)) and the upper bound is reported for Mancos shale by (Chandler *et al.* (2016)), when the fracture propagates perpendicular to the bedding plane.

Predicted breakdown pressures for Shale given the above-mentioned values for ν and K_{Ic} and an average value for ν=0.3 are calculated and listed in Table 2.

Table 2. Fracture toughness and predicted breakdown pressure for shale.

ν	0.15		0.3		0.4	
K_{Ic} [MPa.m$^{0.5}$]	0.47	0.72	0.47	0.72	0.47	0.72
P_b [MPa]	7.2	9.5	26.5	28.8	44.7	46.9

Movie S2.

Neutron radiography showing hydraulic fracture in a shale specimen. The hydraulic fracture is initiated at the top and bottom of the wellbore, propagates along the vertical orientation as the imposed boundary conditions require (plane strain), interacts with pre-existing natural fractures, and as a result activates one of the bedding planes.

Movie S3.

Neutron tomography showing natural fractures within a shale specimen, the hydraulic fracture generated from the wellbore along the vertical direction, and the activated bedding plane near the middle of specimen thickness.

ACKNOWLEDGEMENTS

Authors truly appreciate the precise work of Caltech machine shop (a.k.a. GALCIT shop) technician, Matavos Zargarian, and assistance of the shop manager, Joe Haggerty. Also, assistance provided by the Caltech research engineer, Petros Arakelian is greatly appreciated. The authors would like to acknowledge the kind help of Jelke Dijkstra with the experiments in Grenoble.
Pressure and flow data for fractured samples are available at http://doi.org/10.5281/zenodo.825801.

REFERENCES

Bauer, S., Beyer, C., Dethlefsen, F., Dietrich, P., Duttmann, R., Ebert, M., Feeser, V., Goerke, U., Koeber, R., Kolditz, O., Rabbel, W., Schanz, T., Schafer, D., Wuerdemann, H. & Dahmke, A. (2013). Impacts of the use of the geological subsurface for energy storage: an investigation concept. *Environmental earth sciences* **70**, No. 8, 3935–3943.

Bunger, A. P. & Detournay, E. (2008). Experimental validation of the tip asymptotics for a fluid-driven crack. *Journal of the Mechanics and Physics of Solids* **56**, No. 11, 3101–3115.

Bunger, A. P., Gordeliy, E. & Detournay, E. (2013). Comparison between laboratory experiments and coupled simulations of saucer-shaped hydraulic fractures in homogeneous brittle-elastic solids. *Journal of the Mechanics and Physics of Solids* **61**, No. 7, 1636–1654.

Chandler, M. R., Meredith, P. G., Brantut, N. & Crawford, B. R. (2016). Fracture toughness anisotropy in shale. *Journal of Geophysical Research: Solid Earth* **121**, No. 3, 1706–1729.

Choi, S. R. & Salem, J. A. (1993). Fracture-toughness of pmma as measured with indentation cracks. *Journal of Materials Research* **8**, No. 12, 3210–3217.

Christman, D. R. (1972). Dynamic properties of poly(methyl methacrylate). In *Materials and Structures Laboratory, Manufacturing Development, General Motors Corporation*, Warren, Mishigan: Defense Nuclear Agency, Washington, D. C., p. 48.

da Silva, B. & Einstein, H. (2018). Physical processes involved in the laboratory hydraulic fracturing of granite: Visual observations and interpretation. *Engineering Fracture Mechanics* **191**, 125–142.

Dahi-Taleghani, A. & Olson, J. E. (2011). Numerical modeling of multistranded-hydraulic-fracture propagation: Accounting for the interaction between induced and natural fractures. *SPE Journal* **16**, No. 3, 575–581.

Davletbaev, A., Kovaleva, L. & Babadagli, T. (2014). Heavy oil production by electromagnetic heating in hydraulically fractured wells. *Energy & Fuels* **28**, No. 9, 5737–5744.

Day-Lewis, F. D., Harris, J. M. & Gorelick, S. M. (2002). Time-lapse inversion of crosswell radar data. *Geophysics* **67**, No. 6, 1740–1752.

De Pater, C. & Beugelsdijk, L. J. L. (2005). Experiments and numerical simulation of hydraulic fracturing in naturally fractured rock. In *The 40th U.S. Symposium on Rock Mechanics (USRMS), Anchorage, Alaska*, American Rock Mechanics Association, pp. 1–12, rock mechanics for energy, mineral and infrastructure development in the Northern regions; Alaska rocks.

De Pater, C. J., Cleary, M. P., Quinn, T. S., Barr, D. T., Johnson, D. E. & Weijers, L. (1994). Experimental verification of dimensional analysis for hydraulic fracturing. *SPE Production & Facilities* **9**, No. 4, 230–238.

Dershowitz, W., La Pointe, P. & Cladouhos, T. (1998). Derivation of fracture spatial pattern parameters from borehole data. *International Journal of Rock Mechanics and Mining Science* **35**, No. 4-5, 508, 3rd North American Rock Mechanics Symposium, Cancun, Mexico.

Detournay, E. (2016). Mechanics of hydraulic fractures. *Annual Review of Fluid Mechanics* **48**, 311–339.

Economides, M. J. & Nolte, K. G. (2000). Reservoir stimulation. New York: Wiley, URL https://books.google.com/books?id=rDlQAQAAIAAJ.

Frash, L. P., Carey, J. W. & Viswanathan, H. S. (2016). Notched specimen hydraulic fracturing method for conducting mechanical and hydrological experiments at triaxial reservoir conditions. In *Rock Mechanics/Geomechanics Symposium, American Rock Mechanics Association*, Houston, Texas.

Gale, J. F. W., Reed, R. M. & Holder, J. (2007). Natural fractures in the barnett shale and their importance for hydraulic fracture treatments. *AAPG Bulletin* **91**, No. 4, 603–622.

Gdoutos, E. E. (2006). Fracture mechanics: An introduction. Netherlands: Springer.

Groenenboom, J. & Fokkema, J. T. (1998). Monitoring the width of hydraulic fractures with acoustic waves. *Geophysics* **63**, No. 1, 139–148.

Hubbert, M. K. & Willis, D. G. (1957). Mechanics of hydraulic fracturing, transactions of the american institute of mining and metallurgical. *Transactions of the American Institute of Mining and Metallurgical Engineers* **210**, No. 6, 153–163.

Jia, L. C., Chen, M. & Jin, Y. (2014). 3d imaging of fractures in carbonate rocks using x-ray computed tomography technology.

Carbonates and Evaporites **29**, No. 2, 147–153.

Juhlin, C. (1995). Imaging of fracture zones in the finnsjon area, central sweden, using the seismic reflection method. *Geophysics* **60**, No. 1, 66–75.

Kawamoto, R., Ando, E., Viggiani, G. & Andrade, J. E. (2018). All you need is shape: predicting shear banding in sand with ls-dem. *Journal of the Mechanics and Physics of Solids* **111**, 375–392.

Lecampion, B. & Desroches, J. (2015). Simultaneous initiation and growth of multiple radial hydraulic fractures from a horizontal wellbore. *Journal of the Mechanics and Physics of Solids* **82**, 235–258.

Lecampion, B., Desroches, J., Jeffrey, R. G. & Bunger, A. P. (2017). Experiments versus theory for the initiation and propagation of radial hydraulic fractures in low-permeability materials. *Journal of Geophysical Research: Solid Earth* **122**, No. 2, 1239–1263.

Lee, H. P., Olson, J. E., Holder, J., Gale, J. F. W. & Myers, R. D. (2015). The interaction of propagating opening mode fractures with preexisting discontinuities in shale. *Journal of Geophysical Research: Solid Earth* **120**, No. 1, 169–181.

Legarth, B., Huenges, E. & Zimmermann, G. (2005). Hydraulic fracturing in a sedimentary geothermal reservoir: Results and implications. *International Journal of Rock Mechanics and Mining Sciences* **42**, No. 7, 1028–1041.

Maloszewski, P., Herrmann, A. & Zuber, A. (1999). Interpretation of tracer tests performed in fractured rock of the lange bramke basin, germany. *Hydrology* **7**, No. 2, 209–218.

Maxwell, S. C., Pope, T., Cipolla, C., Mack, M., Trimbitasu, L., Norton, M. & Leonard, J. (2011). Understanding hydraulic fracture variability through integrating microseismicity and seismic reservoir characterization. In *SPE/EAGE European Unconventional Resources Conference & Exhibition - From Potential to Production, Mar. 20-22, Vienna, Austria, Society of Petroleum Engineers*, SPE 144207, Americas unconventional gas, Richardson: TX, Society of Petroleum Engineers, pp. 482–490.

Mayerhofer, M. J., Richardson, M. F., Walker, R. N., Meehan, D. N., Oehler, M. W. & Browning, R. R. (1997). Proppants? we don't need no proppants. In *SPE Annual Technical Conference and Exhibition, San Antonio, Texas*, SPE-38611-MS, pp. 457–464.

Meng, C. & De Pater, C. J. (2011). Acoustic monitoring of hydraulic fracture propagation in pre-fractured natural rocks. *Key Engineering Materials* **452-453**, 833–836.

Nolte, K. G. (1991). Fracturing-pressure analysis for nonideal behavior. *Journal of Petroleum Technology* **43**, No. 2, 210–218.

Olsson, O., Falk, L., Forslund, O., Lundmark, L. & Sandberg, E. (1992). Borehole radar applied to the characterization of hydraulically conductive fracture zones in crystalline rock. *Geophysical Prospecting* **40**, No. 2, 109–142.

Perfect, E., Cheng, C. L., Kang, M., Bilheux, H. Z., Lamanna, J. M., Gragg, M. J. & Wright, D. M. (2014). Neutron imaging of hydrogen-rich fluids in geomaterials and engineered porous media: A review. *Earth-Science Reviews* **129**, 120–135.

Potluri, N. K., Zhu, D. & Hill, A. D. (2005). The effect of natural fractures on hydraulic fracture propagation. In *SPE European Formation Damage Conference, 2005/1/1, Sheveningen, The Netherlands*, Netherlands: Society of Petroleum Engineers.

Rutqvist, J. & Stephansson, O. (2003). The role of hydromechanical coupling in fractured rock engineering. *Hydrogeology Journal* **11**, No. 1, 7–40.

Sone, H. & Zoback, M. D. (2013). Mechanical properties of shale-gas reservoir rockspart 1: Static and dynamic elastic properties and anisotropy. *Geophysics* **78**, No. 5, 381–392.

Song, I., Suh, M., Won, K. S. & Haimson, B. (2001). A laboratory study of hydraulic fracturing breakdown pressure in tablerock sandstone. *Geosciences Journal* **5**, No. 3, 263.

Sun, W., Andrade, J. E., Rudnicki, J. W. & Eichhubl, P. (2011). Connecting microstructural attributes and permeability from 3d tomographic images of in situ shear-enhanced compaction bands using multiscale computations. *Geophysical Research Letters* **38**, connecting microstruc.

Tada, H., Paris, P. C. & Irwin, G. R. (2000). The stress analysis of cracks handbook. ASME Press.

Tsang, C. F., Neretnieks, I. & Tsang, Y. (2015). Hydrologic issues associated with nuclear waste repositories. *Water resources research* **51**, No. 9, 6923–6972.

Van Dam, D. B., De Pater, C. J. & Romijn, R. (2000). Analysis of hydraulic fracture closure in laboratory experiments. *SPE Production and Facilities* **15**, No. 3, 151–158.

Verdon, J. P., Kendall, J. M. & Maxwell, S. C. (2010). A comparison of passive seismic monitoring of fracture stimulation from water and co2 injection. *Geophysics* **75**, No. 3, 1–7.

Viggiani, G., Lenoir, N., Besuelle, P., Di Michiel, M., Marello, S., Desrues, J. & Kretzschmer, M. (2004). X-ray microtomography for studying localized deformation in fine-grained geomaterials under triaxial compression. *Comptes Rendus Mecanique* **332**, No. 10, 819–826.

Warpinski, N. R. & Teufel, L. W. (1987). Influence of geologic discontinuities on hydraulic fracture propagation. *Journal of Petroleum Technology* **39**, No. 2, 209–220.

Weerasooriya, T., Moy, P., Casem, D., Cheng, M. & Chen, W. (2006). Fracture toughness of pmma as a function of loading rate. In *SEM Annual Conference & Exposition on Experimental and Applied Mechanics, Saint Louis, MO, USA*, Springer.

Williams, J. H. & Johnson, C. D. (2004). Acoustic and optical borehole-wall imaging for fractured-rock aquifer studies. *Journal of Applied Geophysics* **55**, No. 1-2, 151–159.

Williams-Stroud, S., Kilpatrick, J., Cornette, B., Eisner, L. & Hall, M. (2010). Moving outside of the borehole: Characterizing natural fractures through microseismic monitoring. *First Break, European Association of Geoscientists & Engineers (EAGE), Houten, Netherlands* **28**, No. 7, 89–94.

Zimmerman, R. W. & Bodvarsson, G. S. (1996). Hydraulic conductivity of rock fractures. *Transport in Porous Media* **23**, No. 1, 1–30.